

End-to-end Adaptive Dynamic Subsampling and Reconstruction for Cardiac MRI

George Yiasemis^{1,2}, Jan-Jakob Sonke^{1,2}, Jonas Teuwen^{1,2,3}
 {g.yiasemis, j.sonke, j.teuwen}@nki.nl

¹ Netherlands Cancer Institute, Amsterdam, Netherlands

² University of Amsterdam, Amsterdam, Netherlands

³ Radboud University Medical Center, Nijmegen, Netherlands

Abstract. Accelerating dynamic MRI is essential for enhancing clinical applications, such as adaptive radiotherapy, and improving patient comfort. Traditional deep learning (DL) approaches for accelerated dynamic MRI reconstruction typically rely on predefined or random subsampling patterns, applied uniformly across all temporal phases. This standard practice overlooks the potential benefits of leveraging temporal correlations and lacks the adaptability required for case-specific subsampling optimization, which holds the potential for maximizing reconstruction quality. Addressing this gap, we present a novel end-to-end framework for adaptive dynamic MRI subsampling and reconstruction. Our pipeline integrates a DL-based adaptive sampler, generating case-specific dynamic subsampling patterns, trained end-to-end with a state-of-the-art 2D dynamic reconstruction network, namely vSHARP, which effectively reconstructs the adaptive dynamic subsampled data into a moving image. Our method is assessed using dynamic cine cardiac MRI data, comparing its performance against vSHARP models that employ common subsampling trajectories, and pipelines trained to optimize dataset-specific sampling schemes alongside vSHARP reconstruction. Our results indicate superior reconstruction quality, particularly at high accelerations.

Keywords: Adaptive MRI Sampling · Dynamic MRI · Accelerated MRI

1 Introduction and Related Work

Magnetic Resonance Imaging (MRI) represents an important clinical imaging modality. However, its inherent slowness and susceptibility to motion artifacts—resulting for instance, from respiratory, bowel, or cardiac movements—pose significant challenges. These challenges hinder the ability to capture dynamic frequency domain measurements, known as k -space, in real-time, often necessitating patient compliance with actions like voluntary breath-holding. To mitigate these issues, accelerated dynamic acquisition techniques, which involve subsampling of the k -space below the Nyquist ratio [12], have been employed.

Recent advancements have seen Deep Learning (DL)-based MRI reconstruction methods significantly outperforming traditional approaches such as Compressed Sensing (CS) [7]. These DL methods excel in reconstructing MRI images

from highly-accelerated measurements [5,21]. Despite the predominant focus on static MRI reconstruction due to limited reference dynamic acquisitions, recent developments have extended to dynamic MRI reconstruction [8,11,20,24,25].

Nonetheless, a critical limitation persists in DL-based dynamic MRI reconstruction. Current methodologies typically rely on predefined, often arbitrary, subsampling patterns, uniformly applied across all temporal phases. This approach overlooks the benefits of exploiting temporal correlations present in adjacent phases and the potential superiority of DL-based learned adaptive sampling schemes. This forms the primary motivation for our project.

It is important to note that learned optimized or adaptive sampling methods do exist for both Cartesian and non-Cartesian acquisitions, though our work focuses exclusively on Cartesian acquisitions. Previous studies have demonstrated the feasibility of learning optimized sampling schemes, trained jointly with a reconstruction network in single [1] or multi-coil settings [26]. In the adaptive case, various DL-based sampling approaches have been proposed in both single [10,16,23] and multi-coil [2,4] scenarios.

Although these methods have primarily been applied to static data, a recent study [13] proposes a method to address dynamic data acquisitions by learning a single optimized dynamic non-Cartesian trajectory, trained alongside a reconstruction model. To the best of our knowledge, this approach is unique in its focus on learning dynamic sampling from training data. Yet, it does not explore *adaptiveness*, leaving the field of adaptive dynamic subsampling unexplored. Our work aims to fill this gap. Our contributions can be summarized as follows:

- We introduce a novel *learned adaptive dynamic subsampling and reconstruction method* for dynamic, multi-coil, Cartesian MRI data. This method integrates an adaptive dynamic sampling model with a sensitivity map prediction module and the deep-learning-based state-of-the-art vSHARP dynamic MRI reconstruction method [22], all trained *end-to-end*. Our approach is designed for simultaneous training across *varying acceleration factors*.
- We propose two dynamic sampling methodologies: one that learns distinct adaptive trajectories for each phase (*phase-specific*) and another that learns a uniform adaptive trajectory for all phases (*unified*), for 1D or 2D sampling.
- We evaluate our pipeline on a multi-coil, dynamic cardiac MRI dataset [18]. Our evaluations include comparisons with pipelines where dynamic subsampling schemes are dataset-optimized or use fixed or random schemes. The results demonstrate superior performance, particularly at higher accelerations.

2 Background

2.1 Accelerated Dynamic MRI Acquisition

Given a sequence of fully sampled dynamic multi-coil k -space data $\mathbf{y} \in \mathbb{C}^{n \times n_c \times n_f}$, the underlying dynamic image $\mathbf{x}^* \in \mathbb{C}^{n \times n_f}$, can be obtained by applying the inverse Fast Fourier transform \mathcal{F}^{-1} :

$$\mathbf{x}^* = \mathcal{F}^{-1}(\mathbf{y}), \quad (1)$$

where $n = n_1 \times n_2$, n_c , and n_f represent the spatial dimensions, the scanner's number of coils, and the number of phases (time-steps) of the dynamic acquisition, respectively. To accelerate the acquisition, the k -space is subsampled. The acquired subsampled dynamic multi-coil k -space $\tilde{\mathbf{y}} \in \mathbb{C}^{n \times n_c \times n_f}$ can be defined by the forward problem:

$$\tilde{\mathbf{y}}_t^k = \mathcal{A}_{A^t, \mathbf{S}^k}(\mathbf{x}_t^*) + \tilde{\mathbf{e}}_t^k, \quad \mathcal{A}_{A^t, \mathbf{S}^k} := \mathbf{U}_{A^t} \mathcal{F} \mathbf{S}^k, \quad k = 1, \dots, n_c, \quad t = 1, \dots, n_f, \quad (2)$$

where \mathbf{U}_M denotes a subsampling operator acting on a set $M \subseteq \Omega$ as follows:

$$\mathbf{z}_M : (\mathbf{z}_M)_i = (\mathbf{U}_M \mathbf{z})_i = \mathbf{z}_i \cdot \mathbb{1}_M(i), \quad i \in \Omega, \quad \mathbf{z} \in \mathbb{C}^{n \times n_c}. \quad (3)$$

Here, $\Omega := \{1, 2, \dots\}$ denotes the sample space comprising all possible sampling options, where $|\Omega|$ equals n_2 or n for 1D (column) sampling and 2D (point) sampling, respectively. \mathcal{F} denotes the forward FFT, $\mathbf{S}^k \in \mathbb{C}^{n \times n}$ the sensitivity map of the k -th coil, and \mathbf{e}_t^k measurement noise.

The acceleration factor R of the acquisition of $\tilde{\mathbf{y}}$ is determined by the dynamic acquisition set $A = \{A^t\}_{t=1}^{n_f} \subset \Omega^{n_f}$:

$$R = \frac{n_f |\Omega|}{\sum_{t=1}^{n_f} |A^t|}, \quad (4)$$

where $|\cdot|$ denotes the cardinality.

2.2 Dynamic MRI Reconstruction

The goal of dynamic MRI reconstruction involves obtaining an approximation of \mathbf{x}^* using $\tilde{\mathbf{y}}$, formulated as a regularized least-squares optimization problem:

$$\hat{\mathbf{x}} = \underset{\mathbf{x} \in \mathbb{C}^{n \times n_f}}{\operatorname{argmin}} \frac{1}{2} \sum_{t=1}^{n_f} \sum_{k=1}^{n_c} \left\| \mathcal{A}_{A^t, \mathbf{S}^k}(\mathbf{x}_t) - \tilde{\mathbf{y}}_t^k \right\|_2^2 + \mathcal{G}(\mathbf{x}), \quad (5)$$

where $\mathcal{G} : \mathbb{C}^{n \times n_f} \rightarrow \mathbb{R}$ represents an arbitrary regularization functional imposing prior reconstruction information. Equation 5 may be solved numerically in an iterative manner by applying unrolled first-order gradient methods [6].

2.3 Problem Definition

Our objectives in this project involve identifying a dynamic subsampling pattern

$$\mathbf{U}_A := (\mathbf{U}_{A^1}, \dots, \mathbf{U}_{A^{n_f}}), \quad (6)$$

that maximizes the information content of the acquired subsampled data $\tilde{\mathbf{y}}$ which is adapted based on some initial dynamic k -space data $\tilde{\mathbf{y}}_{A_0}$, and within the same framework train a DL-based dynamic reconstruction technique. The idea is that both sampling and reconstruction are improved and co-trained by exploiting cross-phase information found across the dynamic data.

3 Methods

3.1 Deep Learning-based Sensitivity Map Prediction

We estimate coil sensitivities utilizing a fully-sampled part of the center of the k -space, also known as the autocalibration signal (ACS), refined through a 2D U-Net-based Sensitivity Map Predictor (SMP), \mathcal{S}_ω . Despite coil sensitivities being ideally phase-independent, we generate maps for all phase data.

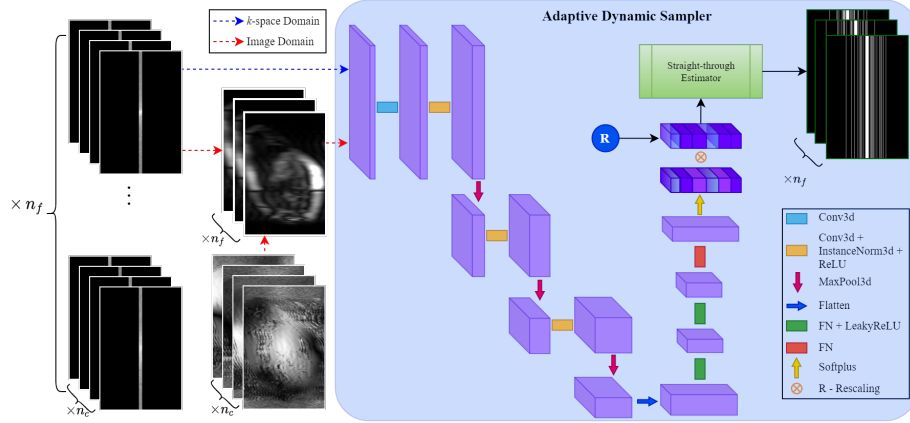


Fig. 1: Adaptive Dynamic Sampler. Here we assume a single cascade ($N = 1$).

3.2 Adaptive Dynamic Sampler

Our approach is designed to allocate a sampling budget online, n_b , derived from the total potential samples, n_a , and an acceleration factor, R ($n_b = n_a/R$). For unified sampling, n_a equals the size of the sample space, $|\Omega|$, while for phase-specific sampling, it is scaled by the number of phases ($n_a := n_f |\Omega|$). We outline our algorithm for phase-specific sampling (for unified sampling set $n_f = 1$).

Algorithm 1: Adaptive Dynamic Sampling

Input: Initial data $\tilde{\mathbf{y}}_{\Lambda_0} \in \mathbb{C}^{n \times n_c \times n_f}$, Acceleration R , Sample Space Ω
Output: Acquisition set $\Lambda = \{\Lambda_N^1, \dots, \Lambda_N^{n_f}\}$

```

1  $n_a \leftarrow n_f |\Omega|$ ;  $n_b \leftarrow n_a / R$ ; // Calculate total budget
2 for  $m \leftarrow 1$  to  $N$  do
3    $n_b^m \leftarrow n_b / N$ ; // Calculate layer budget
4    $p_m \leftarrow \mathcal{M}_{\psi_m} \circ \mathcal{E}_{\theta_m}(\tilde{\mathbf{y}}_{\Lambda_{m-1}})$ ; // Produce adaptive probabilities
5   for  $t \leftarrow 1$  to  $n_f$  do
6     for each  $i \in \Lambda_{m-1}^t$  do;  $(p_m^t)_i \leftarrow 0$ ; // Zero-out already sampled indices
7      $p_m^t \leftarrow \text{Rescale} \circ \text{Softplus}(p_m^t)$ ; // Softplus & Rescale
8      $\Lambda_m^t \leftarrow \text{STE}(p_m^t)$  s.t.  $|\Lambda_m^t| = \frac{m \times n_b}{N \times n_f}$ ; // Produce adaptive sampling

```

Our Adaptive Dynamic Sampler (ADS) incorporates N cascades of encoders, \mathcal{E}_{θ_m} , and multi-layer perceptrons (MLPs), \mathcal{M}_{ψ_m} , dividing the total budget evenly, i.e. n_b/N . Encoder modules mimic a U-Net encoder structure, alternating between l_{enc} 3D convolutional layers ($3 \times 3 \times 3$ kernels) with instance normalization (IN) [15] and ReLU activations, and max-pooling layers ($2 \times 2 \times 2$ kernels), except for the first one. The MLPs consist of l_{mlp} linear layers, each followed by a leaky ReLU (with negative slope 0.01) activation, except for the final layer.

Each \mathcal{E}_{θ_m} receives subsampled measurements as input, which are either reconstructed using sensitivity maps (SENSE) or aggregated across the coil dimension, pertaining to either image or k -space domain encoding. This process results in an encoding that is subsequently flattened and introduced into \mathcal{M}_{ψ_m} , generating probability vectors

$$p_m = (p_m^1, \dots, p_m^{n_f}) \in \mathbb{R}^{n_a} \text{ such that } p_m^t \in \mathbb{R}^{|\Omega|}. \quad (7)$$

Probabilities for previously acquired measurements are set to zero. A softplus activation function is applied to each p_m^t , followed by rescaling to ensure

$$\text{mean}(p_m^t) = \frac{n_b/N}{n_a}, \quad (8)$$

following [1, 23]. Addressing the non-differentiability of the top-k operation, we incorporate a straight-through estimator (STE) for end-to-end training, following [2, 23, 26]. This entails stochastically producing Λ_m^t by binarizing p_m^t through rejection sampling to meet the precise sampling budget ($\frac{n_b}{N \times n_f}$), and utilizing a sigmoid function with a slope of 10 for gradient approximation. It's worth noting that STE is also utilized for inference, allowing for stochasticity.

The first ADS layer processes initial data acquired on Λ_0 (e.g., $\Lambda_0 = \Lambda_{\text{acs}}$), and subsequent layers handle measurements based on previous layer outputs. The m -th layer aims to produce an acquisition set Λ_m , ensuring

$$\Lambda_m \cap \Lambda_{m-1} = \emptyset \quad \text{and} \quad |\Lambda_m^t| = \frac{m \times n_b}{N \times n_f}. \quad (9)$$

Refer to Alg. 1 for a detailed description of our ADS module for phase-specific sampling, further illustrated in Fig. 1.

3.3 Dynamic MRI Reconstruction with vSHARP

Into our pipeline, we incorporate the variable Splitting Half-quadratic ADMM algorithm for Reconstruction of inverse-Problems (vSHARP). We selected vSHARP due to its state-of-the-art performance, as demonstrated by its success in the CM-RxRecon challenge 2023 for dynamic cardiac MRI reconstruction. It effectively solves (5) by employing half-quadratic variable splitting and applies ADMM unrolled optimization over T iterations. Given subsampled measurements $\tilde{\mathbf{y}}$ and sensitivity maps \mathbf{S} , it predicts the underlying dynamic image: $\hat{\mathbf{x}} = \mathcal{R}_\phi(\tilde{\mathbf{y}}; \mathbf{S})$. For additional details see [19,20].

3.4 End-to-end Adaptive Dynamic Sampling and Reconstruction

For our holistic approach to adaptive dynamic subsampling and reconstruction we integrate the methodologies detailed in Sections 3.1, 3.2, and 3.3. The process is visually summarized in Fig. 2 and algorithmically in Alg. 2. Given ACS data $\tilde{\mathbf{y}}_{A_{\text{acs}}}$, the sensitivities \mathbf{S} are predicted via \mathcal{S}_ω . Subsequently, with initial measurements $\tilde{\mathbf{y}}_{A_0}$ and a specified acceleration factor, the adaptive dynamic sampling module $\text{ADS}_{\psi, \theta}$ generates an adaptive dynamic subsampling pattern \mathbf{U}_A . Note that for acceleration consistency we choose $A_{\text{acs}} \subseteq A_0$. After acquiring the data $\tilde{\mathbf{y}}_A$ using the adapted scheme A , \mathcal{R}_ϕ produces a dynamic image reconstruction utilizing \mathbf{S} and $\tilde{\mathbf{y}}_A$. The training of our framework proceeds in an end-to-end (E2E) manner, jointly optimizing the parameters of all three modules

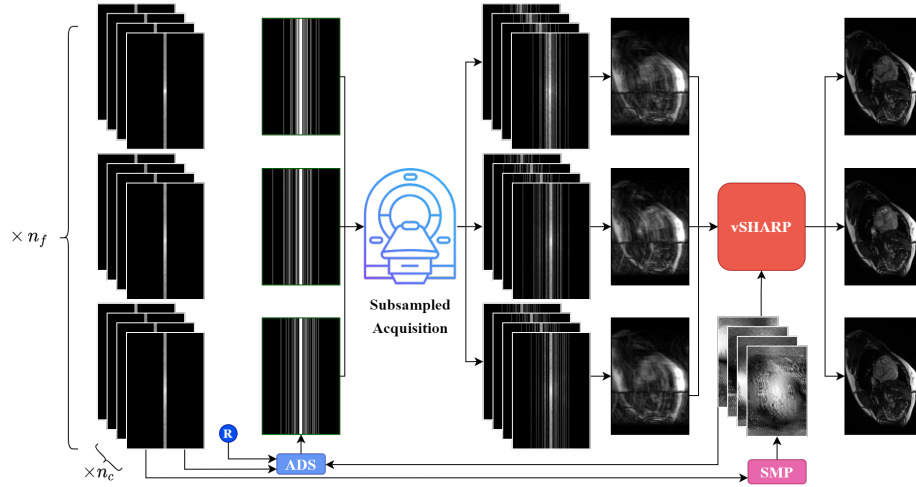


Fig. 2: E2E Adaptive Dynamic Sampling and Reconstruction pipeline.

Algorithm 2: End-to-end Adaptive Dynamic Sampling and Reconstruction**Input:** Initial data $\tilde{\mathbf{y}}_{\Lambda_0}$, ACS data $\tilde{\mathbf{y}}_{\Lambda_{\text{acs}}} : \Lambda_{\text{acs}} \subseteq \Lambda_0$, Acceleration factor R **Output:** Reconstructed image $\hat{\mathbf{x}}$, Adaptive acquisition set Λ

```

1 for  $k \leftarrow 1$  to  $n_c$  do
2   for  $t \leftarrow 1$  to  $n_f$  do
3      $\mathbf{S}_t^k = \mathcal{S}_\omega(\tilde{\mathbf{y}}_{\Lambda_{\text{acs}}}^k)$  ; // Estimate sensitivity maps
4    $\Lambda = \{\Lambda^1, \dots, \Lambda^{n_f}\} = \text{ADS}_{\psi, \theta}(\tilde{\mathbf{y}}_{\Lambda_0}; \mathbf{S}, R)$  ; // Adaptive dynamic pattern
5    $\tilde{\mathbf{y}} = (\tilde{\mathbf{y}}_1, \dots, \tilde{\mathbf{y}}_{n_f}) = (\mathbf{U}_{\Lambda^1}(\mathbf{y}_1), \dots, \mathbf{U}_{\Lambda^{n_f}}(\mathbf{y}_{n_f}))$  ; // Acquire dynamic data
6    $\hat{\mathbf{x}} = \mathcal{R}_\phi(\tilde{\mathbf{y}}; \mathbf{S})$  ; // Reconstruct dynamic image

```

4 Experiments

4.1 Dataset

We utilized the CMRxRecon dataset [18] acquired based on protocols from [17], comprising 473 scans (3185 sequences) of 4D multi-coil cine cardiac k -space data, split into training, validation, and test sets (251, 111, 111 scans, respectively).

4.2 Comparative Studies

To validate our proposed method, we perform the following comparisons for phase-specific or unified subsampling scheme generation:

1. Predetermined or Random schemes including common 1D Random, 1D Gaussian or 1D Equispaced, and 2D Gaussian trajectories.
2. Optimized learned dynamic schemes in both 1D and 2D, employing the same end-to-end process described in 3.2, but substituting our ADS module with a parameterized scheme optimized over the training set (Opt).
3. Our ADS as elaborated in 3.2, in 1D and 2D, initiated with ACS ($\Lambda_0 = \Lambda_{\text{acs}}$).
4. ADS (in 1D) using two equispaced initializations Λ_0 :
 - (i) $\frac{|\Omega|}{|\Lambda_0|} = R - 4$ (Ad-I),
 - (ii) $\frac{|\Omega|}{|\Lambda_0|} = R - 2$ (Ad-I2), including ACS data in Λ_0 , i.e.: $\Lambda_{\text{acs}} \subset \Lambda_0$.

4.3 Ablation Studies

Further validating our approach, we investigated ablative settings (in 1D):

1. ADS considering non-uniformly sampled time-frames, allowing for varied acceleration rates throughout the sequence (Ad-NU).
2. ADS employing a frequency domain encoding sampler, initiated with either ACS (Ad- k) or equispaced ($\Lambda_{\text{acs}} \subset \Lambda_0$, $\frac{|\Omega|}{|\Lambda_0|} = R - 2$, denoted as Ad- k I).

4.4 Experimental Setup

Optimization Models were developed in PyTorch [9], using Adam optimizer with a learning rate starting at 1e-3, linearly increasing to 3e-3 over 2k iterations, then reducing by 20% every 10k iterations, over 52k iterations. Experiments were conducted on NVIDIA A100 and A6000 GPUs, with a batch size of 1. We used a dual-domain loss strategy, combining image and frequency domain losses, over predicted and ground truth images and k -spaces for vSHARP unrolled steps:

$$\mathcal{L} = \sum_{j=1}^T w_j \left[\sum_{t=1}^{n_f} (\mathcal{L}_{\text{SSIM}}(\hat{\mathbf{x}}_t^{(j)}, \mathbf{x}_t^*) + \mathcal{L}_1(\hat{\mathbf{x}}_t^{(j)}, \mathbf{x}_t^*) + \mathcal{L}_{\text{HFEN}}(\hat{\mathbf{x}}_t^{(j)}, \mathbf{x}_t^*) + 3 \cdot \mathcal{L}_{\text{NMAE}}(\hat{\mathbf{y}}_t^{(j)}, \mathbf{y}_t)) + \mathcal{L}_{\text{SSIM3D}}(\hat{\mathbf{x}}^{(j)}, \mathbf{x}^*) \right], \quad w_j = 10^{(j-T)/(T-1)}, \quad (10)$$

where $\{\hat{\mathbf{x}}^{(j)}\}_{j=1}^T$ and $\{\hat{\mathbf{y}}^{(j)}\}_{j=1}^T$ represent the series of predicted images and k -space data, respectively. The definitions for $\mathcal{L}_{\text{SSIM}}$, \mathcal{L}_1 , $\mathcal{L}_{\text{HFEN}}$, $\mathcal{L}_{\text{NMAE}}$, follow those specified in [22], and $\mathcal{L}_{\text{SSIM3D}}$ is an extension of $\mathcal{L}_{\text{SSIM}}$ for 3D data.

Hyperparameter Settings In our adaptive sampling experiments, we configured the ADS sampler with $N = 2$ cascades. Unless specified otherwise, we use image domain encoding ADS modules. Our setup features encoders with $l_{\text{enc}} = 3$ scales and MLPs with $l_{\text{mlp}} = 3$ layers each. For optimized sampling, we employed an identical pipeline as our end-to-end approach by replacing the sampler model with a n_a -dimensional parameter representing Ω (n_a defined as in Sec. 3.2). In all our experiments the SMP module comprised a 2D U-Net with 4 scales (16, 32, 64, 128 channels) and we used vSHARP as detailed in [20] with $T = 8$ and 3D U-Nets as denoisers composed of 4 scales (16, 32, 64, 128 channels).

Subsampling All experiments used a fraction $r_{\text{acs}} := |\Lambda_{\text{acs}}| = 4\%$ of Ω to fully sample the ACS k -space, i.e., $\tilde{\mathbf{y}}_{\Lambda_{\text{acs}}}$ which is used for sensitivity map prediction. During training the acceleration was randomly chosen between 4, 6, 8, while for inference we also evaluated our setups on acceleration factors of 4, 6 and 8.

Evaluation Models were evaluated using SSIM, PSNR, and NMSE metrics, as outlined in [22], averaged per slice or phase within a scan. For significance tests, we use the Almost Stochastic Order test [3,14] with $\alpha = 0.05$.

5 Results

	Method	4x	6x	8x
Fixed	Gauss	0.9930	0.9911	0.9885
	Rand	0.9921	0.9900	0.9874
	Equi	0.9933	0.9909	0.9881
Learned	Opt	0.9936	0.9895	0.9878
	Adapt	0.9936	0.9917	0.9887
	Ad-I	0.9934	0.9916	0.9895
	Ad-I2	0.9936	0.9921	0.9900
	Ad-NU	0.9938	0.9919	0.9884
	Ad- k	0.9934	0.9913	0.9876
	Ad- k I2	0.9936	0.9918	0.9897

Table 1: Phase-specific SSIM results (1D)

	Method	4x	6x	8x
Fix	Gauss	0.9956	0.9948	0.9939
	Opt	0.9963	0.9953	0.9943
Lrn	Adapt	0.9965	0.9957	0.9948

Table 2: Phase-specific SSIM results (2D)

	Method	4x	6x	8x
Fixed	Gauss	0.9851	0.9788	0.9712
	Rand	0.9798	0.9720	0.9696
	Equi	0.9882	0.9809	0.9708
Learned	Opt	0.9880	0.9820	0.9775
	Adapt	0.9877	0.9830	0.9780
	Ad-I	0.9880	0.9838	0.9775
	Ad-I2	0.9888	0.9838	0.9768

Table 3: Unified SSIM results (1D)

	Method	4x	6x	8x
Fix	Gauss	0.9954	0.9943	0.9930
	Opt	0.9958	0.9944	0.9928
Lrn	Adapt	0.9962	0.9952	0.9937

Table 4: Unified SSIM results (2D)

* **Bold** numbers indicate the best method, while **colored** numbers indicate a significant difference compared to the best method.

Tables 1 to 4, and Supplementary Tables S1 to S4 detail the average SSIM, pSNR, and NMSE metrics for our most successful checkpoints evaluated on the validation set within each configuration. These findings highlight the superior performance of phase-specific sampling approaches over unified strategies across all evaluated techniques, acceleration factors, and sampling dimensions.

Notably, our Adaptive Dynamic Sampling method stands out in both phase-specific and unified scenarios, as well as in both sampling types—line and point sampling—demonstrating superior performance with statistical significance in most experiments across all metrics. Specifically, under all configurations, the highest-performing method is a variant of our proposed ADS approach.

A notable improvement in the ADS method was achieved by integrating equispaced initializations along with ACS data (Ad-I, Ad-I2) into the adaptive 1D sampling strategy, significantly boosting the performance of the ADS module in the majority of evaluations. Moreover, our method’s enhanced performance is especially marked at higher acceleration factors, in both phase-specific and unified scenarios, highlighting the adaptiveness of our sampling strategies.

Figure 3, Supplementary Fig. S1 and S3 showcase examples of phase-specific sampling patterns, whereas Supplementary Fig. S2 and S4 illustrate unified sampling strategies from our studies. Visual inspections reveal a tendency towards selecting low-frequency components in both optimized and ADS methods under phase-specific conditions. Nevertheless, ADS occasionally incorporates higher

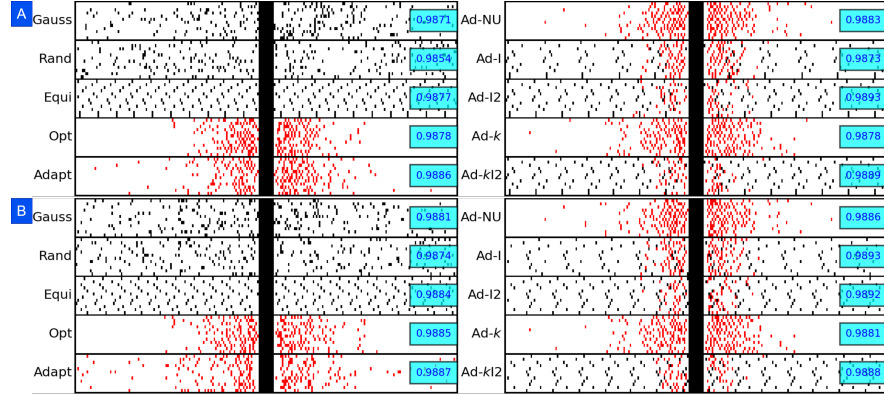


Fig. 3: Example of patterns across setups for phase-specific (each phase represented by one row) setups at $R = 8$ for two cases. Black: fixed/initial pattern, red: learned pattern. Cyan boxes mark SSIM values.

frequencies and creates distinct sampling patterns for consecutive time-frames, showcasing its capability to effectively leverage information shared across phases.

6 Conclusion

This study presents an end-to-end framework combining adaptive dynamic subsampling with dynamic reconstruction, assessed using dynamic cardiac MRI data. By integrating a DL-based adaptive dynamic sampler with a state-of-the-art reconstruction network, our approach notably outperforms both traditional and DL-optimized methods. By generating adaptive sampling schemes that exploit correlations across phases (phase-specific) or unified (one pattern for all phases), our approach is robust to high acceleration factors while ensuring high-quality image reconstruction, motivating real-time dynamic subsampled acquisitions. Although this study’s retrospective nature did not extend to testing the physical implementation within an MRI scanner, future investigations should explore the practical application of our proposed methods. Implementing phase-specific schemes might face challenges such as large gradient switches and eddy currents, unlike in the unified scenario, where such issues are less likely to arise.

References

1. Bahadir, C.D., Dalca, A.V., Sabuncu, M.R.: Learning-Based Optimization of the Under-Sampling Pattern in MRI, p. 780–792. Springer International Publishing (2019). https://doi.org/10.1007/978-3-030-20351-1_61 2, 5
2. Bakker, T., Muckley, M.J., Romero-Soriano, A., Drozdal, M., Pineda, L.: On learning adaptive acquisition policies for undersampled multi-coil MRI reconstruction. In: Medical Imaging with Deep Learning (2022) 2, 5
3. Del Barrio, E., Cuesta-Albertos, J.A., Matrán, C.: An optimal transportation approach for assessing almost stochastic order. In: The Mathematics of the Uncertain, pp. 33–44. Springer (2018) 8
4. Gautam, S., Li, A., Ravishankar, S.: Patient-adaptive and learned mri data under-sampling using neighborhood clustering (2024) 2
5. Guo, P., Mei, Y., Zhou, J., Jiang, S., Patel, V.M.: Reconformer: Accelerated mri reconstruction using recurrent transformer. IEEE transactions on medical imaging (2023) 2
6. Liang, D., Cheng, J., Ke, Z., Ying, L.: Deep magnetic resonance image reconstruction: Inverse problems meet neural networks. IEEE Signal Processing Magazine **37**(1), 141–151 (Jan 2020). <https://doi.org/10.1109/msp.2019.2950557> 3
7. Lustig, M., Donoho, D.L., Santos, J.M., Pauly, J.M.: Compressed sensing mri. IEEE signal processing magazine **25**(2), 72–82 (2008) 1
8. Lønning, K., Caan, M.W., Nowee, M.E., Sonke, J.J.: Dynamic recurrent inference machines for accelerated mri-guided radiotherapy of the liver. Computerized Medical Imaging and Graphics p. 102348 (2024). <https://doi.org/https://doi.org/10.1016/j.compmedimag.2024.102348> 2
9. Paszke, A., Gross, S., Chintala, S., Chanan, G., Yang, E., DeVito, Z., Lin, Z., Desmaison, A., Antiga, L., Lerer, A.: Automatic differentiation in pytorch (2017) 8
10. Pineda, L., Basu, S., Romero, A., Calandra, R., Drozdal, M.: Active mr k-space sampling with reinforcement learning. In: Martel, A.L., Abolmaesumi, P., Stoyanov, D., Mateus, D., Zuluaga, M.A., Zhou, S.K., Racocanu, D., Joskowicz, L. (eds.) Medical Image Computing and Computer Assisted Intervention – MICCAI 2020. pp. 23–33. Springer International Publishing, Cham (2020) 2
11. Qin, C., Schlemper, J., Caballero, J., Price, A.N., Hajnal, J.V., Rueckert, D.: Convolutional recurrent neural networks for dynamic mr image reconstruction. IEEE Transactions on Medical Imaging **38**(1), 280–290 (Jan 2019). <https://doi.org/10.1109/tmi.2018.2863670> 2
12. Shannon, C.: Communication in the presence of noise. Proceedings of the IRE **37**(1), 10–21 (1949). <https://doi.org/10.1109/JRPROC.1949.232969> 1
13. Shor, T.: Multi PILOT: Feasible learned multiple acquisition trajectories for dynamic MRI. In: Medical Imaging with Deep Learning (2023) 2
14. Ulmer, D., Hardmeier, C., Frellsen, J.: deep-significance-easy and meaningful statistical significance testing in the age of neural networks. arXiv preprint arXiv:2204.06815 (2022) 8
15. Ulyanov, D., Vedaldi, A., Lempitsky, V.: Improved texture networks: Maximizing quality and diversity in feed-forward stylization and texture synthesis. In: 2017 IEEE Conference on Computer Vision and Pattern Recognition (CVPR). pp. 4105–4113 (2017). <https://doi.org/10.1109/CVPR.2017.437> 5
16. Van Gorp, H., Huijben, I., Veeling, B.S., Pezzotti, N., Van Sloun, R.J.G.: Active deep probabilistic subsampling. In: Meila, M., Zhang, T. (eds.) Proceedings of

- the 38th International Conference on Machine Learning. Proceedings of Machine Learning Research, vol. 139, pp. 10509–10518. PMLR (18–24 Jul 2021) [2](#)
17. Wang, C., Li, Y., Lv, J., Jin, J., Hu, X., Kuang, X., Chen, W., Wang, H.: Recommendation for cardiac magnetic resonance imaging-based phenotypic study: Imaging part. *Phenomics* **1**(4), 151–170 (Jul 2021). <https://doi.org/10.1007/s43657-021-00018-x> [7](#)
 18. Wang, C., et al.: Cmrrecon: An open cardiac mri dataset for the competition of accelerated image reconstruction (2023). <https://doi.org/10.48550/ARXIV.2309.10836> [2](#), [7](#)
 19. Yiasemis, G., Moriakov, N., Sonke, J.J., Teuwen, J.: vsharp: variable splitting half-quadratic admm algorithm for reconstruction of inverse-problems (2023). <https://doi.org/10.48550/ARXIV.2309.09954>, <https://arxiv.org/abs/2309.09954> [6](#)
 20. Yiasemis, G., Moriakov, N., Sonke, J.J., Teuwen, J.: Deep cardiac mri reconstruction with admm. In: Camara, O., Puyol-Antón, E., Sermesant, M., Suinesiaputra, A., Tao, Q., Wang, C., Young, A. (eds.) *Statistical Atlases and Computational Models of the Heart. Regular and CMRxRecon Challenge Papers*. pp. 479–490. Springer Nature Switzerland, Cham (2024). https://doi.org/10.1007/978-3-031-52448-6_45 [2](#), [6](#), [8](#)
 21. Yiasemis, G., Sonke, J.J., Sánchez, C., Teuwen, J.: Recurrent variational network: A deep learning inverse problem solver applied to the task of accelerated mri reconstruction. In: *Proceedings of the IEEE/CVF Conference on Computer Vision and Pattern Recognition (CVPR)*. pp. 732–741 (June 2022) [2](#)
 22. Yiasemis, G., Sánchez, C.I., Sonke, J.J., Teuwen, J.: On retrospective k-space subsampling schemes for deep mri reconstruction. *Magnetic Resonance Imaging* **107**, 33–46 (2024). <https://doi.org/https://doi.org/10.1016/j.mri.2023.12.012> [2](#), [8](#)
 23. Yin, T., Wu, Z., Sun, H., Dalca, A.V., Yue, Y., Bouman, K.L.: End-to-end sequential sampling and reconstruction for mr imaging. In: *Proceedings of the Machine Learning for Health Conference* (2021) [2](#), [5](#)
 24. Yoo, J., Jin, K.H., Gupta, H., Yerly, J., Stuber, M., Unser, M.: Time-dependent deep image prior for dynamic mri. *IEEE Transactions on Medical Imaging* **40**(12), 3337–3348 (Dec 2021). <https://doi.org/10.1109/tmi.2021.3084288> [2](#)
 25. Zhang, C., Caan, M., Navest, R., Teuwen, J., Sonke, J.: Radial-rim: accelerated radial 4d mri using the recurrent inference machine. In: *Proceedings of International Society for Magnetic Resonance in Medicine*. vol. 31 (2023) [2](#)
 26. Zhang, J., Zhang, H., Wang, A., Zhang, Q., Sabuncu, M., Spincemaille, P., Nguyen, T.D., Wang, Y.: Extending loupe for k-space under-sampling pattern optimization in multi-coil mri (2020) [2](#), [5](#)

Supplementary Material for ‘End-to-end Adaptive Dynamic Subsampling and Reconstruction for Cardiac MRI’

A Supplementary Tables

Method		R = 4		R = 6		R = 8	
		pSNR	NMSE	pSNR	NMSE	pSNR	NMSE
Fixed	Gauss	49.34	0.0032	47.94	0.0043	46.21	0.0065
	Rand	48.59	0.0038	47.14	0.0053	45.70	0.0074
	Equi	49.98	0.0027	48.10	0.0042	46.34	0.0063
Learned	Opt	49.45	0.0031	45.46	0.0078	44.81	0.0090
	Adapt	49.63	0.0030	47.94	0.0043	45.75	0.0072
	Ad-I	49.69	0.0029	48.22	0.0041	46.79	0.0057
	Ad-I2	50.05	0.0027	48.53	0.0038	47.07	0.0053
	Ad-NU	49.72	0.0029	48.01	0.0043	45.48	0.0077
	Ad-k	49.59	0.0030	47.74	0.0046	45.17	0.0082
	Ad-kI2	49.83	0.0028	48.38	0.0039	46.97	0.0054

Table S1: Phase-spec. pSNR & NMSE results (1D)

Method	R = 4		R = 6		R = 8		
	pSNR	NMSE	pSNR	NMSE	pSNR	NMSE	
Fix	Gauss	52.41	0.0015	51.49	0.0019	50.62	0.0023
	Opt	53.68	0.0012	52.33	0.0019	51.22	0.0020
Lrn	Adapt	54.01	0.0011	52.83	0.0014	51.59	0.0019

Table S2: Phase-spec. pSNR & NMSE results (2D)

Method	R = 4		R = 6		R = 8		
	pSNR	NMSE	pSNR	NMSE	pSNR	NMSE	
Fixed	Gauss	45.49	0.0077	43.07	0.0133	40.85	0.0221
	Rand	43.75	0.0117	41.45	0.0200	40.62	0.0233
	Equi	47.32	0.0052	44.49	0.0104	41.24	0.0203
Learned	Opt	46.29	0.0064	42.59	0.0150	41.63	0.0187
	Adapt	46.59	0.0060	43.74	0.0115	42.31	0.0159
	Ad-I	46.69	0.0059	44.62	0.0093	42.49	0.0151
	Ad-I2	47.35	0.0050	44.92	0.0087	42.55	0.0149

Table S3: Unified pSNR & NMSE results (1D)

Method	R = 4		R = 6		R = 8		
	pSNR	NMSE	pSNR	NMSE	pSNR	NMSE	
Lrn Fix	Gauss	52.12	0.0016	51.00	0.0021	49.98	0.0027
	Opt	53.40	0.0012	51.61	0.0018	50.23	0.0025
	Adapt	53.62	0.0012	52.16	0.0016	50.46	0.0024

Table S4: Unified pSNR & NMSE results (2D)

* **Bold** numbers indicate the best method, while **colored** numbers indicate a significant difference compared to the best method.

B Supplementary Figures

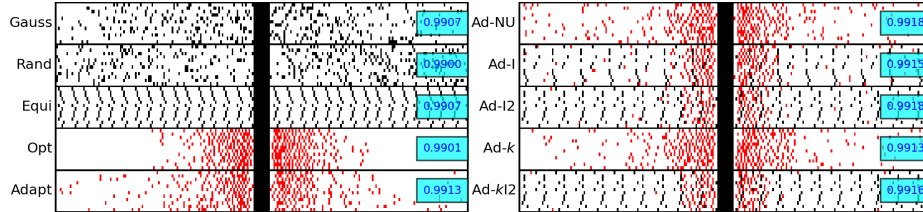


Fig.S1: Example of patterns from phase-specific setups for 1D sampling at $R = 6$. Each row represents a scheme per phase. Black: Fixed/Initial scheme. Red: Learned scheme.

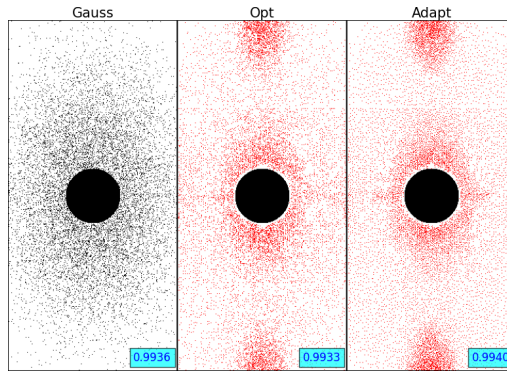


Fig. S2: Example of masks across setups for unified 2D sampling setups at $R = 8$. Black: fixed/initial pattern, red: learned pattern. Cyan boxes mark SSIM values.

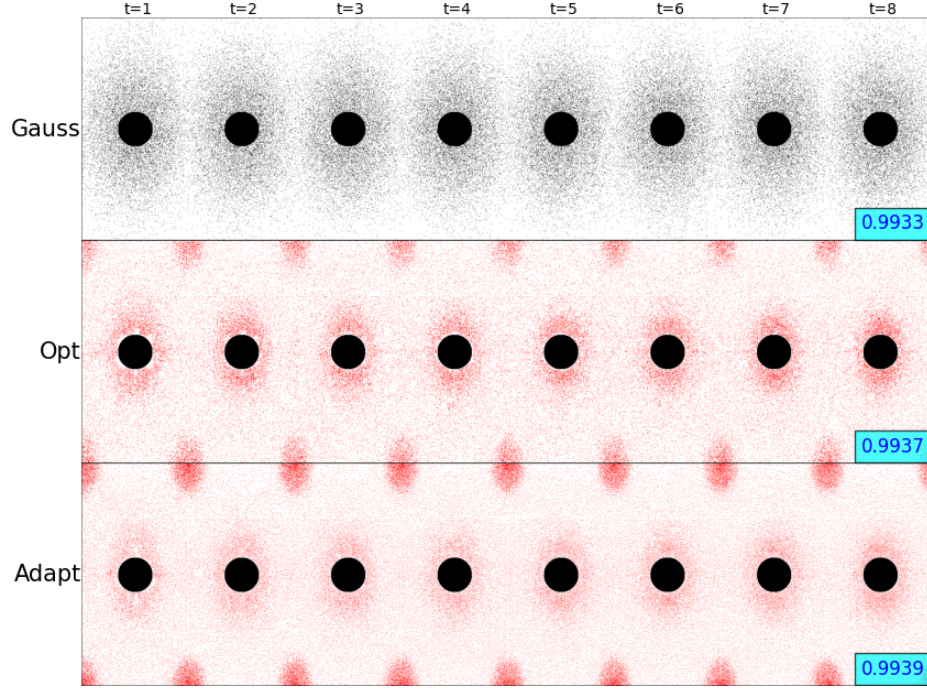


Fig.S3: Example of masks from phase-specific (first 8 phases) setups for 2D sampling at $R = 8$. Black: Fixed/Initial scheme. Red: Learned scheme.

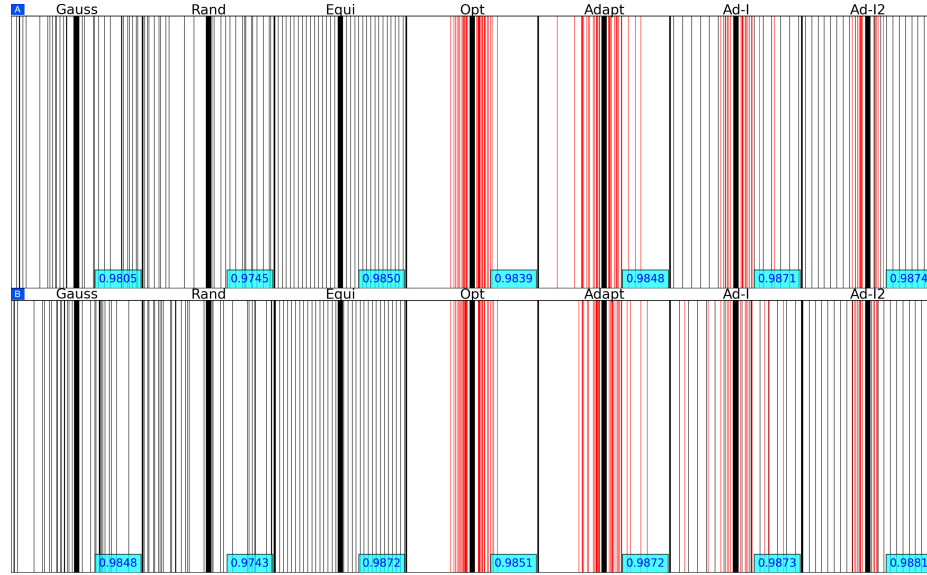


Fig.S4: Example of masks from unified setups for 1D sampling at $R = 6$ or two cases. Black: Fixed/Initial scheme. Red: Learned scheme. Cyan boxes indicate reconstruction SSIM metric.